

Cosmological Constraints on Horndeski Gravity in Light of GW170817

C. D. Kreisch^{a,b,1} and E. Komatsu^{b,c}

^aPrinceton University,
4 Ivy Lane, Princeton, NJ 08544 USA

^bMax-Planck-Institut für Astrophysik,
Karl-Schwarzschild Strasse 1, 85748 Garching, Germany

^cKavli Institute for the Physics and Mathematics of the Universe (Kavli IPMU, WPI), Todai
Institutes for Advanced Study, University of Tokyo,
Kashiwa 277-8583, Japan

E-mail: ckreisch@astro.princeton.edu, komatsu@mpa-garching.mpg.de

Abstract. The discovery of the electromagnetic counterpart to GW170817 severely constrains the tensor mode propagation speed, eliminating a large model space of Horndeski theory. We use the cosmic microwave background data from Planck and the joint analysis of the BICEP2/Keck Array and Planck, galaxy clustering data from the SDSS LRG survey, BOSS baryon acoustic oscillation data, and redshift space distortion measurements to place constraints on the remaining Horndeski parameters. We evolve the Horndeski parameters as power laws with both the amplitude and power law index free. We find a 95% CL upper bound on the present-day coefficient of the Hubble friction term in the cosmological propagation of gravitational waves is 2.38, whereas General Relativity gives 2 at all times. While an enhanced friction suppresses the amplitude of the reionization bump of the primordial B-mode power spectrum at $\ell < 10$, our result limits the suppression to be less than 0.8%. This constraint is primarily due to the scalar integrated Sachs-Wolfe effect in temperature fluctuations at low multipoles.

¹Corresponding author.

Contents

1	Introduction	1
2	Modeling & Data Sets	2
3	Stability Constraints	4
4	Results	5
5	Sources of Constraints	7
5.1	Cosmic Microwave Background	8
5.1.1	Scalar Perturbations	8
5.1.2	Tensor Perturbations	10
5.2	Large Scale Structure	10
6	Discussion	12
7	Summary	14
A	Model Specifics	15
B	Effects of Kineticity on Stability Constraints	16
C	Parameter Evolution	19

1 Introduction

The detection of gravitational waves opens a new window into constraining gravity. In general relativity (GR), the line element for scalar mode perturbations in the Newtonian gauge is given by $ds^2 = a^2(\tau) [-(1 + 2\Psi) d\tau^2 + (1 - 2\Phi) dx^2]$. The line element for tensor mode perturbations is $ds^2 = a^2(\tau) [-d\tau^2 + (\delta_{ij} + h_{ij}) dx^i dx^j]$, where $h_{ij} = \pm h_+, h_\times$ are small perturbations and are the divergenceless, traceless component of the metric. The linearized Einstein equation without a source takes the form of the wave equation $\square h_{ij} = 0$, where \square is the D'Alembertian. Then, going to Fourier space, the gravitational waves can be described by $\ddot{h}_{ij} + 2\frac{\dot{a}}{a}\dot{h}_{ij} + k^2 h_{ij} = 0$, where k is the wavenumber. Dots throughout the paper denote derivatives with respect to conformal time.

Changing the gravitational theory modifies the propagation of gravitational waves. In Horndeski theory, the most general tensor-scalar theory in which the equations of motion are second order [1], the tensor mode propagation equation becomes

$$\ddot{h}_{ij} + [2 + \alpha_M(a)] \mathcal{H} \dot{h}_{ij} + c_T^2(a) k^2 h_{ij} = 0, \quad (1.1)$$

using the parameterization developed by [2] and where $\mathcal{H} = \dot{a}/a$. The Planck mass run rate α_M describes how the Planck mass evolves over time and contributes to the gravitational wave friction. It is defined as

$$\alpha_M = \frac{d \ln (M_*^2)}{d \ln a}, \quad (1.2)$$

where M_*^2 is the effective Planck mass. If not constant, α_M creates anisotropic stress in the Jordan frame.

The tensor speed c_T is given by $c_T^2 = 1 + \alpha_T$, where α_T is the tensor speed excess that quantifies how much the gravitational wave speed deviates from that of light. Recent observations of GW170817 and its electromagnetic counterpart have placed the stringent bounds

$$-6 \times 10^{-15} \leq \alpha_0^T \leq 1.4 \times 10^{-15}. \quad (1.3)$$

This new constraint effectively eliminates all Horndeski theories with $\alpha_0^T \neq 0$ and alters the physically allowed values of the other Horndeski parameters [3]. See e.g. [4] for an example of a non-trivial theory compatible with $c_T = c$, [5, 6] for discussions of how gravitational wave detections impact Horndeski theory, [7, 8, 9] for good theoretical discussions about the impact of GW170817, and [10] for observational constraints on Horndeski theory using only the simultaneous detection of GW170817 and GRB170817A. In this paper we use measurements of the cosmic microwave background (CMB), galaxy clustering, baryon acoustic oscillations (BAO), and redshift space distortions (RSD) to constrain the remaining Horndeski parameters in light of this discovery.

The remaining viable tensor mode propagation equation is

$$\ddot{h}_{ij} + [2 + \alpha_M(a)] \mathcal{H} \dot{h}_{ij} + k^2 h_{ij} = 0. \quad (1.4)$$

Two additional parameters, the kineticity α_K and braiding α_B , complete the parameterized Horndeski theory. Kineticity describes the scalar perturbations' kinetic energy. Large values reduce the scalar sound speed. The kinetic braiding parameter describes how the scalar and metric kinetic terms mix [see e.g. 11, 12, 13, for good discussions]. A nonzero value indicates the clustering of dark energy. All four parameters are independent of each other and the background, which we choose to be Λ CDM. Λ CDM GR cosmology is regained when all $\alpha_i = 0$.

In Section 2 we discuss our parameterization of the Horndeski parameters and what data we use to constrain them, and in Section 3 we define the model's stability constraints. We present our results in Section 4 and discuss the source of constraining power in Section 5. In Section 6 we compare our models and discuss our results. We summarize in Section 7. In Appendix A we provide additional background information about Horndeski's theory and its implementation. Appendix B details how kineticity affects the model's stability constraints and how this influences our results, and in Appendix C we discuss our evolution of the Horndeski parameters.

2 Modeling & Data Sets

We use EFTCAMB¹ [14, 15], a modified version of the Boltzmann code CAMB [16] that does not use a quasi-static approximation, as well as the complimentary CosmoMC version [17], to study the effects of modified gravity on perturbations. See Appendix A for further detail on how the parameters are handled in the code. We set $R - 1 \lesssim 0.03$, where R is the Gelman-Rubin diagnostic [18], as our criterion to obtain convergence in the chains.

¹<http://www.eftcamb.org/codes/download.html>, version 2.0

To explore the time evolution of the remaining Horndeski parameters and achieve a sufficiently large stable parameter space to perform an MCMC analysis (see Appendix B), we evolve the Horndeski parameters as power laws:

$$\alpha_K = \alpha_0^K a^\kappa \tag{2.1}$$

$$\alpha_B = \alpha_0^B a^\xi \tag{2.2}$$

$$\widetilde{M} = \widetilde{M}_0 a^\beta \implies \alpha_M = \frac{d \ln (M_*^2)}{d \ln a} = \widetilde{M}_0 a^\beta \frac{\beta}{1 + \widetilde{M}_0 a^\beta}, \tag{2.3}$$

where $M_*^2/m_0^2 = 1 + \widetilde{M}$ in the context of EFTCAMB, and m_0^2 is the Planck mass. \widetilde{M}_0 is the fractional deviation of M_*^2 from m_0^2 today. α_0^i denotes the parameter value today, and a is the scale factor. This parameterization is similar to that used by the Planck collaboration for the Horndeski parameters [19]. While we do not know the exact functional form of the α_i 's, Ref. [20] discusses the challenges of parameterizing them as a function of Ω_{DE} and Ref. [21] finds that evolving the α_i 's as power laws, with both the amplitude and power law index free, is preferred over evolving them with simpler or more complex models.

The authors of [12] parameterized the Horndeski parameters as a function of the dark energy density and found that α_K could not be well constrained [see also 22]. To limit the number of additional degrees of freedom in our analysis, we fix the evolution of α_K with $\alpha_0^K = 0.1$ and $\kappa = 3$. We also choose to explore the case of $\alpha_0^B = 0$ to probe a theory in which the primary modification is due to gravitational waves. Fixing $\alpha_0^B = 0$ yields a perfect-fluid model that includes anisotropic stress [2]. If both $\alpha_0^K = 0$ and $\alpha_0^B = 0$, the scalar propagation speed diverges. For this reason we fix the kineticity at a nonzero value throughout our analysis. See Appendix B for a discussion of how kineticity affects the stable parameter space given the imposed stability conditions defined in Section 3. We vary the standard cosmological parameters $\Omega_b h^2$, $\Omega_c h^2$, θ , τ , $\ln(10^{10} A_s)$, n_s , as well as the tensor-to-scalar ratio r , Planck calibration y_{cal} , the dust power ($\ell = 80$, $\nu = 353$ GHz) $A_{B,\text{dust}}$, and the dust frequency scaling parameter $\beta_{B,\text{dust}}$. We choose not to vary w_0 and w_a to minimize the number of free parameters in our analysis and to focus on the propagation of gravitational waves. In Table 1 we list our adopted prior cutoffs for the different parameters. All parameters have uniform priors except for y_{cal} and $\beta_{B,\text{dust}}$, which have the Gaussian priors $y_{\text{cal}} = 1.0000 \pm 0.0025$ and $\beta_{B,\text{dust}} = 1.59 \pm 0.11$, respectively.

Given the direct effect the Horndeski parameters have on tensor perturbations [see Equation 1.4 and e.g. 23, 24, 25], we include in our analysis the B-mode data from the joint analysis of the BICEP2/Keck Array and Planck [26]. Because the Horndeski parameters influence the scalar perturbations, as well, we use the 2015 Planck low- ℓ CMB temperature and polarization data, high- ℓ temperature data, and the lensing potential measurements [27, 28].

It is reasonable to posit the CMB places optimal constraints on the remaining Horndeski parameters at the epoch of decoupling. We studied the optimal pivot scale to measure α_B and α_M and find that they are uncorrelated at present and are best constrained at late times rather than during recombination. See Appendix C for a further discussion. The constraints primarily come from the late integrated Sachs-Wolfe (ISW) effect (see Section 5). The pivot scale is model dependent, however, and should be re-examined when the evolution of the Horndeski parameters is better determined. To take advantage of this late time sensitivity, we include the SDSS LRG DR4 [mpk, 29] and BOSS BAO and RSD data sets in our MCMC analysis [30, 31, 32, 33].

Table 1. Adopted MCMC Priors

Parameter	Prior
\widetilde{M}_0	$[-1, 5]$
β	$[0, 20]$
α_0^B	$[-7, 2]$
ξ	$[0, 20]$
$\Omega_b h^2$	$[0.005, 0.100]$
$\Omega_c h^2$	$[0.001, 0.990]$
$100\theta_{MC}$	$[0.5, 10]$
τ	$[0.01, 0.80]$
$\ln(10^{10} A_s)$	$[2, 4]$
n_s	$[0.8, 1.2]$
r	$[0, 1]$
y_{cal}	$[0.9, 1.1]$
$A_{B,dust}$	$[0, 15]$
$\beta_{B,dust}$	$[1.04, 2.14]$

3 Stability Constraints

Several viability priors can be set by EFTCAMB to ensure the parameter space yields a stable theory. We enforce the following constraints [see 2, 14, 34, for a full description]:

1. Physical stability: the theory must have a positive effective Newton’s constant (i.e., $1 + \Omega > 0$), and avoid ghost and gradient instabilities. Ghost instabilities arise when the kinetic energy becomes negative, and gradient instabilities occur when the squared speed of sound for perturbations becomes negative [see §3.3 of 2, 14].
2. Mathematical stability: neither the coefficient of \ddot{h}_{ij} nor the coefficient of $\ddot{\pi}$ may equal 0, ensuring the tensor perturbation and π field equations are well defined, respectively [14, 34, 35]. In this work we exclude all exponential growth of the π field perturbations, including those due to tachyon instabilities². For details of the mathematical stability conditions, see Equations 40 and 52 in [34], as well as the corresponding π field equation discussion in section IV D and viability condition discussion in section IV F of [34].
3. We require a positive matter density and dark energy density with $\omega_{DE} \leq -1/3$ at all times.

We do not restrict our analysis to regions of parameter space where $c_s^2 \leq 1$ or $m_\pi^2 \geq 0$. Subluminal sound speeds are required for the theory to be UV complete through standard methods [2, 37]. The authors of [38] have shown, however, that Horndeski theories will always

²Some argue that tachyon instabilities are not harmful because they produce perturbation growth on large scales which is, thus, bounded [see e.g. 36]. In contrast are gradient instabilities that produce unbounded perturbation growth on small scales. Nevertheless, in this paper we follow the framework of EFTCAMB, in which the mathematical stability conditions include the tachyon stability requirement.

have regions of parameter space that include superluminal sound speeds [see also 2, for a brief discussion]. If the scalar field couples to matter, its speed and mass are more complicated to compute than if the field were in a vacuum. They cannot be directly read from the π propagation equation because the scalar degree of freedom of the theory is a combination of π and the matter fields. Enforcing $c_s^2 \leq 1$ in EFTCAMB would not put a limit on the true scalar sound speed in the non-minimal coupling scenario [39]. We note that restrictions on c_s can have a severe impact on the stable parameter space. The authors of [40] have shown that restricting the scalar field to propagate subluminally yields a stable parameter space that is a very small subsection of the parameter space allowed when the scalar field is free to have any real sound speed.

4 Results

In Figure 1 and Figure 2 we show the resulting posterior probability distributions for the cases with $\alpha_0^B \neq 0$ and $\alpha_0^B = 0$, respectively. CMB denotes the low- ℓ TEB, high- ℓ TT [27], and BKP [26] data set combination. LSS denotes combining the lensing [28], mpk [29], BAO [30, 31], and RSD [32, 33] data sets. Constraints on the friction and braiding parameters are quoted in Table 2 and Table 3. See [41] for constraints on α_B from galaxy cluster observations in light of the observation of the electromagnetic counterpart to GW170817.

One may be surprised to see that the bounds on \widetilde{M}_0 and α_0^M exclude their GR values at 95% confidence in the case of $\alpha_0^B \neq 0$. However, these lower bounds are driven largely by stability constraints on the model when $\alpha_0^K = 0.1$. For this kineticity, as $\widetilde{M}_0 \rightarrow 0^+$, $\alpha_0^B \rightarrow 0^+$, as well. Thus, for the $\alpha_0^B \neq 0$ case, there is not a large enough stable region around $\widetilde{M}_0 = 0$ for the posterior to show a nonzero probability.

α_0^M has an upper limit of 0.38 and 0.41 at 95% confidence for $\alpha_0^B \neq 0$ and $\alpha_0^B = 0$, respectively, for the CMB+LSS data sets. The stable parameter space for \widetilde{M}_0 is large (see Appendix B), so the upper 95% CL constraints for this parameter are driven by data. Matter clustering and the late ISW effect are both sensitive probes of \widetilde{M}_0 (see Section 5).

For $\alpha_0^B = 0$, \widetilde{M}_0 and α_0^M are consistent with GR. See also the bimodal posterior for \widetilde{M}_0 in Figure 2 when $\alpha_0^B = 0$. When $\alpha_0^B = 0$, \widetilde{M}_0 is stable at 0 and values near 0, allowing for the bimodal posterior in Figure 2. The posterior is bimodal rather than smooth because there is a small number of stable parameter values when $0 \lesssim \widetilde{M}_0 \lesssim 0.1$. Indeed, the \widetilde{M}_0 posterior for the $\alpha_0^B \neq 0$ case and the rightmost mode in the posterior for the $\alpha_0^B = 0$ case rise near $\widetilde{M}_0 = 0.1$.

The shape of this stable parameter region near $\widetilde{M}_0 = 0$ is purely driven from the choice of α_0^K . When $\alpha_0^K = 0$, values between $\widetilde{M}_0 = 0$ and $\widetilde{M}_0 \approx 0.1$ are stable, eliminating the bottleneck effect in the $\widetilde{M}_0 - \alpha_0^B$ stable space as $\widetilde{M}_0 \rightarrow 0^+$. However, to investigate the case of $\alpha_0^B = 0$, α_0^K must be nonzero since $\alpha_0^B = 0$ and $\alpha_0^K = 0$ simultaneously are unstable. See Appendix B for a further discussion.

Both ξ , the power law index for the braiding parameter, and β , the power law index related to friction, are relatively unconstrained by the data. In fact, ξ cannot be constrained at the 95% CL for the $\alpha_0^B \neq 0$ case with CMB data alone. At 68% confidence, $\xi > 2.82$ for this case. Note that the nonzero probability for $\xi = 0$ in Figure 1 is due to smoothing artifacts. The constraints on β are almost purely from stability constraints (see Appendix B). There is a small stable region for β near 0 if ξ is near 0, but the data did not prefer this region. The β posterior bounds in Figure 1 and Figure 2 correspond to the boundaries of the

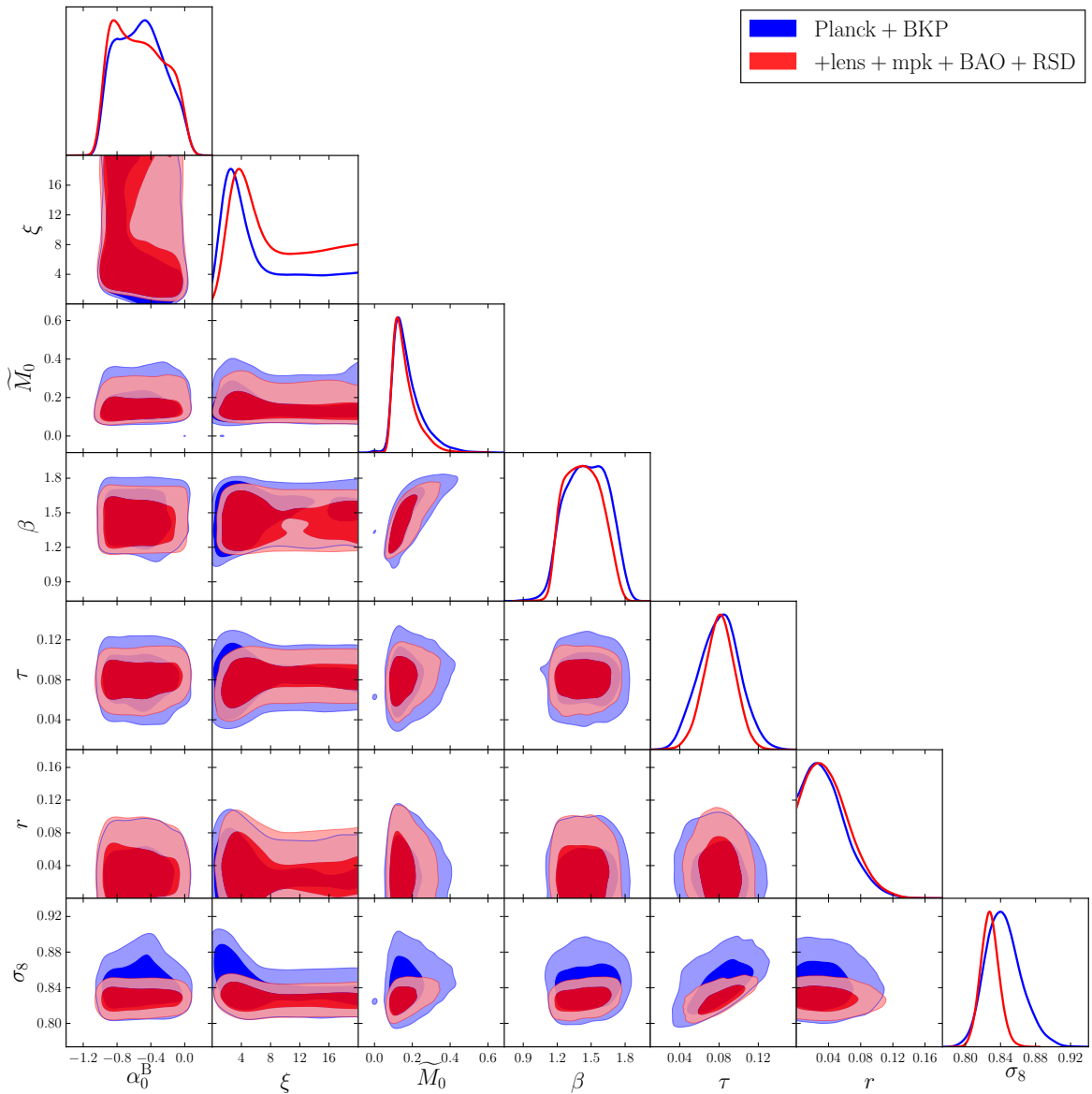


Figure 1. Constraints on the Horndeski parameters, τ , r , and σ_8 for $\alpha_0^K = 0.1$ and $\alpha_0^B \neq 0$.

remaining portion of the stable parameter space. ξ has a large stable parameter space, so the best-fit appears driven by the data. However, the plateau in the posterior for large ξ is due to the data being unable to further constrain the parameter.

Larger values of β are preferred for larger \widetilde{M}_0 . This suggests that, for a power law evolution, the data prefer to minimize the deviation from m_0^2 at early times. The $\xi - \alpha_0^B$ contour in Figure 1 shows a similar trend for $\xi \lesssim 2$ as α_0^B deviates farther from 0.

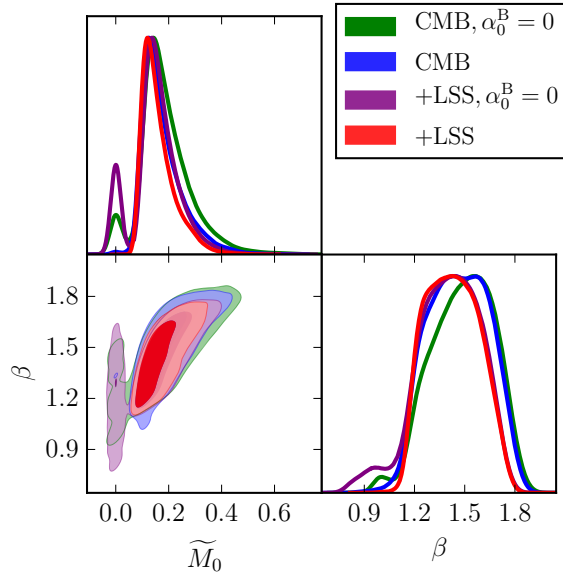


Figure 2. Constraints on the Horndeski friction parameters for $\alpha_0^K = 0.1$ and both braiding cases. The bimodality in the \widetilde{M}_0 posterior is due to stability constraints. We note that smoothing for plotting purposes reduces the amplitude of the leftmost mode.

Table 2. Parameter 95% Confidence Limits, $\alpha_0^B \neq 0$

Parameter	Planck + BKP	+ lens + mpk + BAO + RSD
\widetilde{M}_0	$0.17^{+0.18}_{-0.11}$	$0.160^{+0.14}_{-0.091}$
β	$1.46^{+0.32}_{-0.31}$	$1.43^{+0.28}_{-0.27}$
α_0^M	$0.22^{+0.23}_{-0.16}$	$0.20^{+0.18}_{-0.12}$
α_0^B	$-0.53^{+0.50}_{-0.46}$	$-0.54^{+0.52}_{-0.46}$
ξ	–	> 2.16

Table 3. Parameter 95% Confidence Limits, $\alpha_0^B = 0$

Parameter	Planck + BKP	+ lens + mpk + BAO + RSD
\widetilde{M}_0	$0.18^{+0.21}_{-0.21}$	$0.14^{+0.18}_{-0.18}$
β	$1.49^{+0.33}_{-0.34}$	$1.40^{+0.36}_{-0.45}$
α_0^M	$0.23^{+0.25}_{-0.26}$	$0.18^{+0.23}_{-0.22}$

5 Sources of Constraints

Where do the constraints on the Horndeski parameters come from? To identify the source of dominating constraining power, we compute power spectra derivatives at our fiducial cos-

mology for the temperature, E-mode polarization, B-mode polarization, lensing potential, and matter power spectra in Figures 3-6. Our fiducial values for the Horndeski parameters, tensor-to-scalar ratio, and tensor tilt are listed in Table 4, and we use the best-fit Planck TT+lowP+lensing+ext Λ CDM parameter values [42]. The fiducial Horndeski values were chosen based on the posteriors in Figure 1 and Figure 2. Computing the relative difference between the Horndeski and fiducial (rather than GR) spectra ensures all the spectra have a stable theory while only varying a single parameter.

The power spectra are most affected at large scales by the Horndeski parameters, and the CMB scalar modes and large scale structure (LSS) are significantly more sensitive to these parameters than the CMB tensor modes.

Table 4. Fiducial Parameters

Parameter	Value
α_0^K	0.1
κ	3.0
α_0^B	-0.5
ξ	3.0
\widetilde{M}_0	0.15
β	1.5
r	0.05
n_t	0

5.1 Cosmic Microwave Background

5.1.1 Scalar Perturbations

In Figure 3 we show the sensitivity of the unlensed temperature and polarization anisotropies to changes in the Horndeski parameters in the neighborhood of the fiducial parameters, which is a good proxy for the constraining power near the best-fit values. In general, the CMB anisotropies are most sensitive to the Horndeski parameters at $\ell \lesssim 10$, though measurements at such scales are limited by cosmic variance. The perturbations are most sensitive to the friction parameter \widetilde{M}_0 , and \widetilde{M}_0 has a more dramatic effect on the scalar temperature anisotropies than on polarization, lensing, and matter clustering.

The sensitivity of the scalar TT power spectrum to the Horndeski parameters at low- ℓ suggests the ISW effect may be the source of sensitivity. In Figure 4 we show power spectra derivatives with and without the ISW effect. Removing the ISW effect erases any sensitivity the scalar TT power spectrum had to the Horndeski parameters, including braiding, indicating the ISW effect is the primary source of constraint for the temperature anisotropies. Because a nonzero Planck-mass run rate creates anisotropic stress, the evolution of the Bardeen potentials changes over time [36, 43]. The anisotropic stress constraint from the spatial traceless component of the Einstein equations makes this clear [2]:

$$\Psi - \Phi - \alpha_M H v_X = \tilde{p}_m \pi_m, \quad (5.1)$$

where $v_X = -\frac{a\delta\phi}{\phi}$ is the scalar velocity potential, and $H = \mathcal{H}/a$. Friction alters the relationship between the Bardeen potentials, leading to a change in the ISW and, thus, the temperature anisotropies. As seen in Figure 4, increasing braiding decreases the ISW effect,

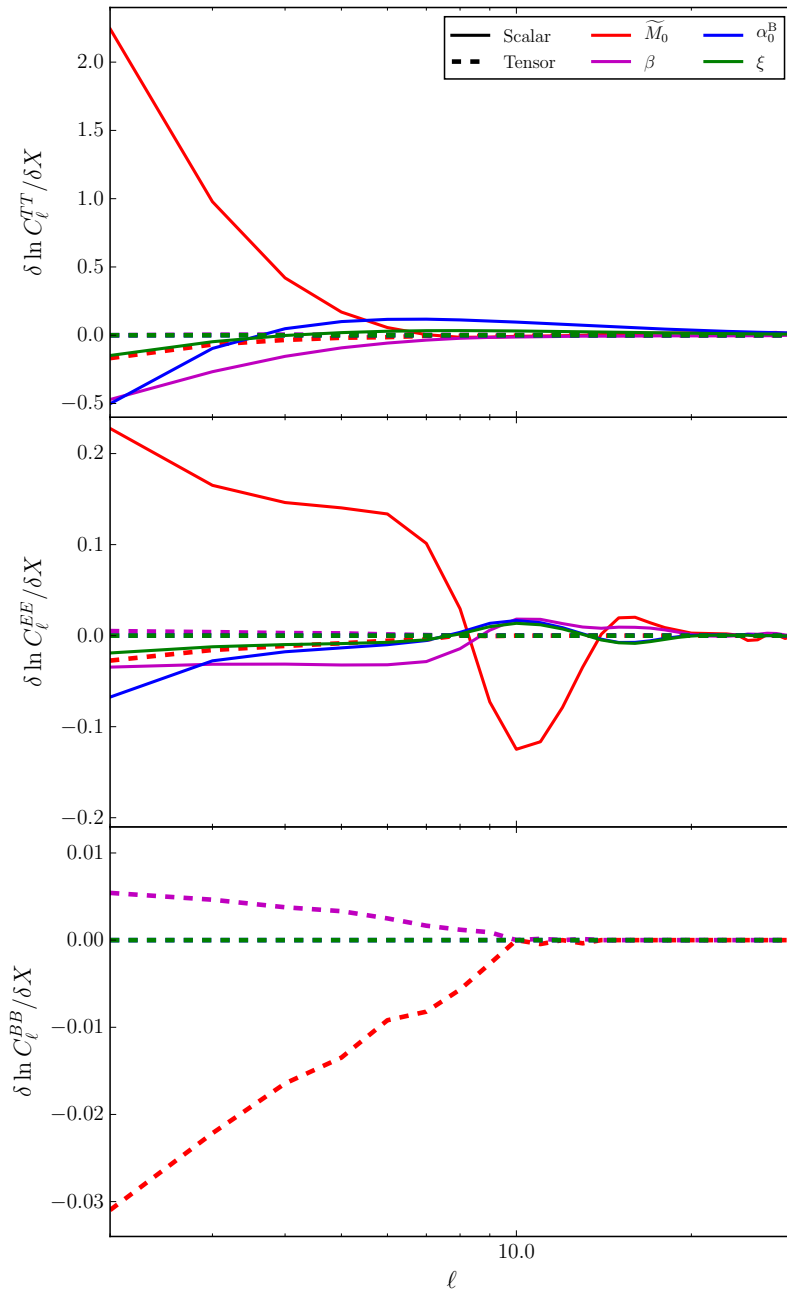


Figure 3. Sensitivity of the CMB perturbations to the Horndeski parameters as a function of scale. Colors denote which Horndeski parameter was varied while all other parameters were held constant. Solid (dashed) lines correspond to scalar (tensor) modes. Note that what is shown is equivalent to the derivative of a fractional deviation, i.e. $\frac{1}{C_\ell} \delta C_\ell / \delta X$.

reducing the power of the temperature anisotropies at low- ℓ [see 43, for a further discussion of α_M , α_B , and the ISW effect].

Friction's effect on the temperature anisotropies via the ISW also changes the local

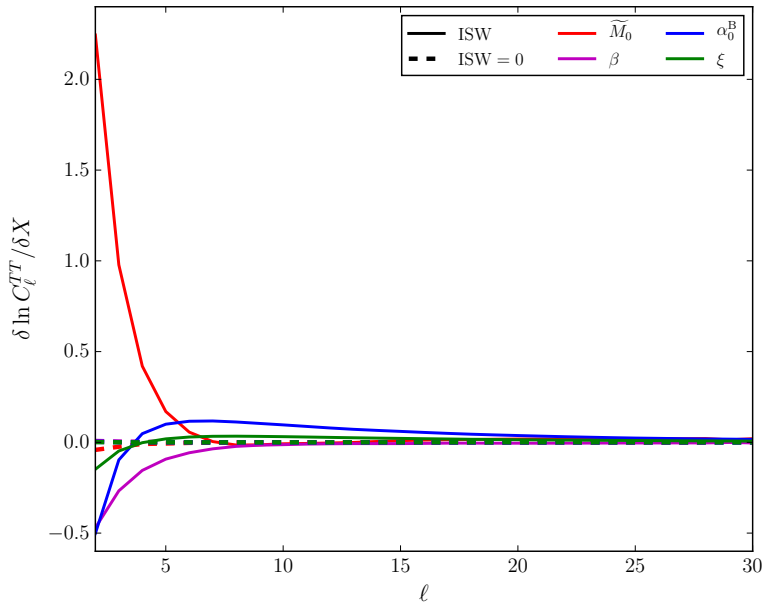


Figure 4. Sensitivity of the ISW effect to the Horndeski parameters as a function of scale. Colors denote which Horndeski parameter was varied while all other parameters were held constant. Solid (dashed) lines correspond to including (excluding) the ISW. Removing the ISW from the TT power spectrum eliminates the sensitivity of the temperature anisotropies to the Horndeski parameters.

temperature quadrupole seen by electrons during reionization, altering the low- ℓ E-mode. Scattering of the reionization electrons off the quadrupole produces additional polarization at the scale that enters the horizon during reionization. Increasing \widetilde{M}_0 makes the reionization bump peakier for the scalar E-modes, boosting the power for $\ell < 10$ and damping the power near $\ell = 10$.

5.1.2 Tensor Perturbations

Braiding only affects the scalar modes. Increasing the friction term \widetilde{M}_0 dampens the tensor perturbations, decreasing the B-mode and tensor E-mode amplitudes (see middle and bottom panels in Figure 3). This is expected since the form of Equation 1.4 is that of a damped driven oscillator [see also 25, 44]. For the tensor mode polarization, increasing \widetilde{M}_0 decreases the reionization bump. See e.g. [23] and [25] for a further discussion on how friction affects the reionization peak.

Only gravitational waves outside the horizon at recombination affect the temperature anisotropies since the gravitational waves decay and oscillate as soon as they enter the horizon. Since friction is a damping term for the gravitational waves, the tensor temperature power spectrum is damped for low- ℓ , as well. Nonetheless, friction has a more dramatic effect on the scalar modes, so the scalar temperature and E-mode polarization dominate the CMB constraints.

5.2 Large Scale Structure

Increasing friction damps the lensing potential at all scales, but most significantly at large angular scales (see Figure 5). This occurs because $|\Phi + \Psi|$ is damped from increasing the

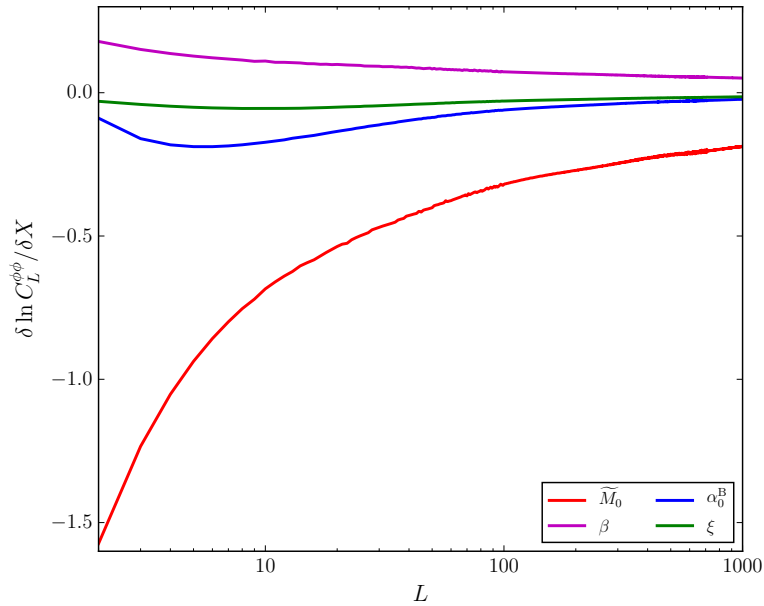


Figure 5. Sensitivity of the lensing potential to the Horndeski parameters. Colors denote which Horndeski parameter was varied while all other parameters were held constant.

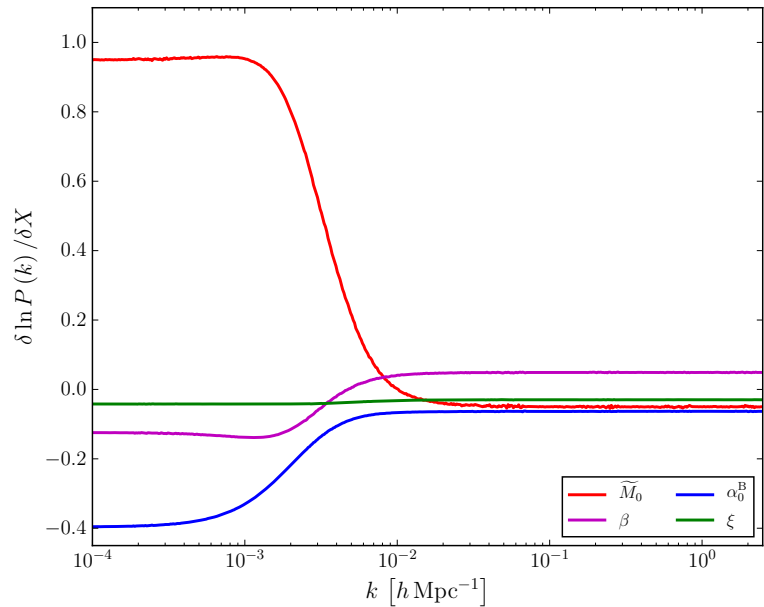


Figure 6. Sensitivity of matter clustering to the Horndeski parameters. Colors denote which Horndeski parameter was varied while all other parameters were held constant.

friction. The lensing potential is almost as sensitive to the friction parameters as the scalar TT power spectrum at large scales, but present lensing potential measurements do not cover

Table 5. Model Comparison: Values of $\Delta\text{AIC} = \text{AIC}_{\alpha_{\text{B}} \neq 0} - \text{AIC}_{\alpha_{\text{B}} = 0} = \Delta\chi^2 + 4$

Observable	Planck + BKP	+ lens + mpk + BAO + RSD
BKP	3.95	4.02
high- ℓ TT	2.63	3.95
low- ℓ TEB	3.40	3.75
lens	–	3.86
mpk	–	3.96
BAO	–	3.99
RSD	–	4.18
Total	1.97	3.72

multipoles $L < 40$ and so the lensing potential does not have strong constraining power.

Both α_{B} and α_{M} alter the growth rate [2]. In the neighborhood of our fiducial cosmology, increasing \widetilde{M}_0 boosts clustering for $k \lesssim 10^{-2} h \text{Mpc}^{-1}$ (see Figure 6). Increasing α_0^{B} so that it is closer to GR reduces clustering on similar scales. The matter power spectrum shows weak sensitivity to the Horndeski parameters for the scales directly probed by the LSS measurements. The dominating constraining power on the Horndeski parameters from these measurements comes through their constraints on σ_8 .

6 Discussion

To compare the two models we can use the Akaike information criterion (AIC) [45], defined as:

$$\text{AIC} = -2\ln(\mathcal{L}) + 2k = \chi^2 + 2k, \quad (6.1)$$

where $\chi^2 = \chi_{\text{BKP}}^2 + \chi_{\text{high-}\ell\text{TT}}^2 + \chi_{\text{low-}\ell\text{TEB}}^2$ for the CMB data set combination and $\chi^2 = \chi_{\text{BKP}}^2 + \chi_{\text{high-}\ell\text{TT}}^2 + \chi_{\text{low-}\ell\text{TEB}}^2 + \chi_{\text{lens}}^2 + \chi_{\text{mpk}}^2 + \chi_{\text{BAO}}^2 + \chi_{\text{RSD}}^2$ for the CMB+LSS data set combination. Then,

$$\Delta\text{AIC} = \text{AIC}_{\alpha_{\text{B}} \neq 0} - \text{AIC}_{\alpha_{\text{B}} = 0} = \Delta\chi^2 + 4 \quad (6.2)$$

where \mathcal{L} is the maximum-likelihood and k is the number of fit parameters, yielding $\Delta\text{AIC} = 1.97$ for the CMB data sets and $\Delta\text{AIC} = 3.72$ after including large scale structure measurements. The AIC takes into account how well the model fits the data while incorporating a penalty proportional to the number of parameters fit. When comparing two models, the lower AIC corresponds to the preferred model. In principle, the Bayes factor should be used to compare the models and the AIC proves only an approximation to it [see, e.g., the introduction of 46, for the Bayes factor].

In Table 5 we list the individual ΔAIC values for each data set used in the CMB and CMB+LSS combinations, as well as the total ΔAIC value for both combinations. All ΔAIC values are positive, indicating the $\alpha_{\text{B}} = 0$ model is preferred for all data sets. For this case the data are consistent with GR.

Incorporating the LSS data leads to a lower preferred value and upper bound on \widetilde{M}_0 (see Table 2 and Table 3). Increasing \widetilde{M}_0 boosts the power of the matter power spectrum for large scales, increasing σ_8 (see Figure 6). A weak correlation between \widetilde{M}_0 and σ_8 is visible in

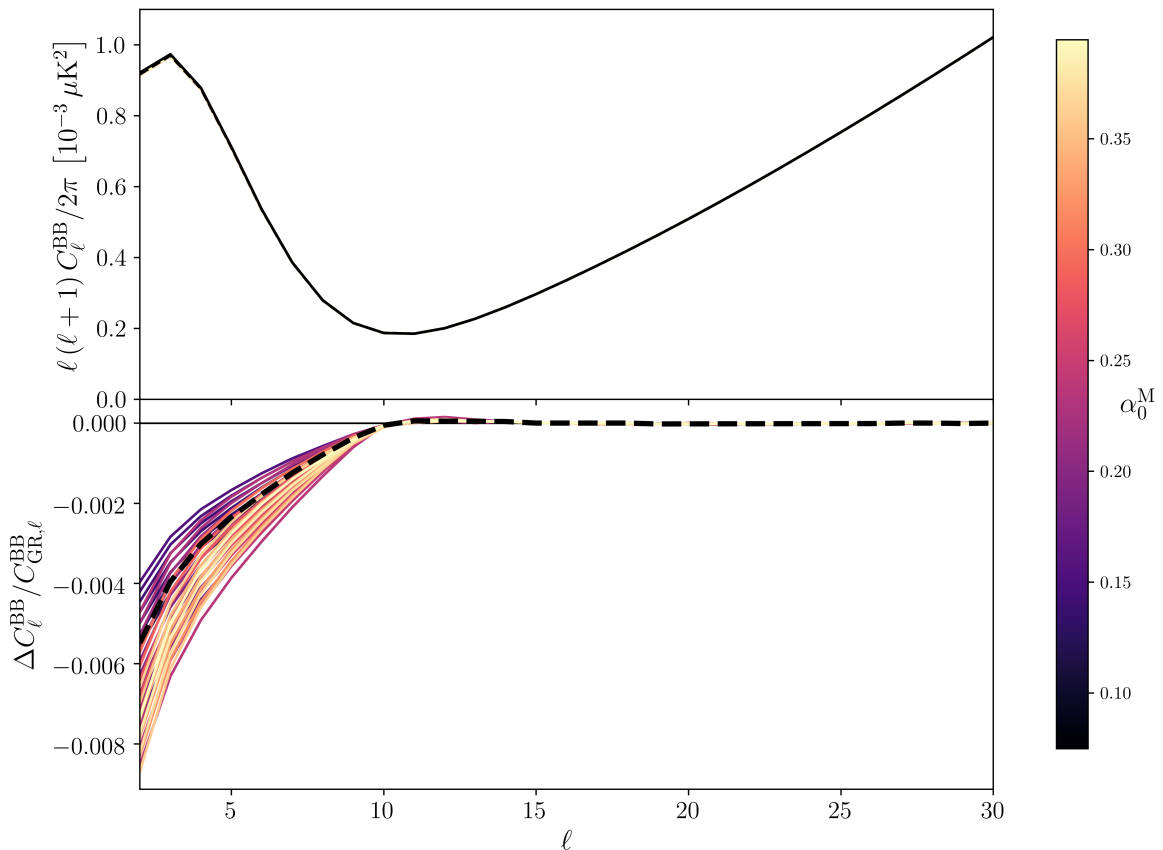


Figure 7. Primordial B-mode spectra for different values of α_0^M allowed at the 95% CL by the CMB+LSS data sets for $\alpha_0^B \neq 0$ with all other parameters fixed. The bottom panel shows the relative difference to GR. The dashed line corresponds to the best-fit values of \tilde{M}_0 and β , the power law index related to friction, for the CMB+LSS data sets for $\alpha_0^B \neq 0$.

the lower boundary of the relevant contour in [Figure 1](#). The RSD measurement’s preference for a lower σ_8 helps shrink the contour and leads to a slightly lower preferred \tilde{M}_0 .

A primary goal of current and future CMB polarization experiments is to make the first detection of B-mode polarization from primordial gravitational waves. With our constraints we can investigate the impact of the Horndeski parameters on such experiments. In [Figure 7](#) we plot the primordial B-modes while varying α_0^M in the 95% CL range allowed by the CMB+LSS data set combination for $\alpha_0^B \neq 0$ to show the range of B-mode spectra consistent with the data. We use $r = 0.05$, $n_t = 0$, the best-fit Planck TT+lowP+lensing+ext Λ CDM parameter values [\[42\]](#), and our best-fit α_0^B and ξ , the power law index for braiding, values for the CMB+LSS data set combination. Even for the largest α_0^M allowed by the data, the deviations from GR are less than 1% at the reionization bump at $\ell < 10$, which is smaller than the cosmic variance. Thus, even without a detection of primordial B-modes to date, we can conclude that the effect of the Horndeski parameters on the primordial B-mode polarization is constrained to be insignificant.

7 Summary

With a fixed kineticity of $\alpha_K = 0.1a^3$ we have shown:

- The friction α_0^M has a 95% CL upper limit of 0.38 and 0.41 when $\alpha_0^B \neq 0$ and $\alpha_0^B = 0$, respectively, when using both CMB and LSS data.
- The lower 95% CL limit for α_0^M excludes GR for the $\alpha_0^B \neq 0$ case but not for the $\alpha_0^B = 0$ case. We believe this is primarily due to tachyon instabilities (defined in Section 3) imposed by fixing $\alpha_0^K = 0.1$.
- The effects of Horndeski theory on primordial B-modes are constrained by CMB and LSS data to be insignificant with 95% confidence.

It is important to remember that even when using Horndeski theory, making different assumptions about the α_i parameters can yield dramatically different results. See e.g. the tight α_0^M constraint by [19], the negative values allowed by [25], [12], and [22], and the constraints found by [40]. We stress that choice of kineticity has a non-negligible impact on the constraints for the other Horndeski parameters due to its effects on the viable parameter space.

The observation of the electromagnetic counterpart to GW170817 has constrained $-6 \times 10^{-15} \leq \alpha_0^T \leq 1.4 \times 10^{-15}$, which seems to eliminate all Horndeski theories with $\alpha_T \neq 0$. Typically, the α_i 's are parameterized so that they are 0 in the matter dominated era and only have late time effects [see e.g. 20, 21]. However, the evolution of α_T could take a form such that $\alpha_T \rightarrow 0$ as $z \rightarrow 0$, but where $\alpha_T \neq 0$ in the past. In this case, Equation 1.1 is still viable. The power law evolution probed in this paper does not permit this behavior, but other functional forms can. It would be interesting to explore the parameter space and constraints from such a theory.

Acknowledgments

CK would like to thank the referee for their very helpful comments, as well as Marco Raveri, Paul Steinhardt, Anna Ijjas, Alexandre Barreira, Kris Pardo, and Alice Pisani for useful discussions. This work was partially funded through a DAAD (German Academic Exchange Service) Research Grant and the National Science Foundation Graduate Research Fellowship, NSF award number DGE1656466.

A Model Specifics

The effective field theory action in unitary gauge and Jordan frame is defined as [47, 48, 49]

$$\begin{aligned}
S = \int d^4x \sqrt{-g} & \left\{ \frac{m_0^2}{2} [1 + \Omega(\tau)] R + \Lambda(\tau) - a^2 c(\tau) \delta g^{00} \right. \\
& + \frac{M_2^4(\tau)}{2} (a^2 \delta g^{00})^2 - \frac{\bar{M}_1^3(\tau)}{2} a^2 \delta g^{00} \delta K^\mu{}_\mu \\
& - \frac{\bar{M}_2^2(\tau)}{2} (\delta K^\mu{}_\mu)^2 - \frac{\bar{M}_3^2(\tau)}{2} \delta K^\mu{}_\nu \delta K^\nu{}_\mu + \frac{a^2 \hat{M}^2(\tau)}{2} \delta g^{00} \delta R^{(3)} \\
& \left. + m_2^2(\tau) (g^{\mu\nu} + n^\mu n^\nu) \partial_\mu (a^2 g^{00}) \partial_\nu (a^2 g^{00}) + \dots \right\} \\
& + S_m[\chi_i, g_{\mu\nu}]
\end{aligned} \tag{A.1}$$

where

$$a^2 \delta g^{00} = a^2 g^{00} + 1, \tag{A.2}$$

$$\delta K^\mu{}_\nu = K^\mu{}_\nu - K^{\mu 0}{}_\nu, \tag{A.3}$$

$$\delta K^\mu{}_\mu = K^\mu{}_\mu - K^{\mu 0}{}_\mu, \tag{A.4}$$

$$\text{and } \delta R^{(3)} = R^{(3)} - R^{(3)0} \tag{A.5}$$

are the perturbations to the time-time metric component, extrinsic curvature, curvature trace, and the three dimensional spatial Ricci scalar, respectively. n^μ is the normal to surfaces of constant time. We adopt EFTCAMB's definitions for clarity. Ω , Λ , and c are the background evolution equations, as a function of conformal time [14, 15]. The background equations Λ and c can be written as a function of Ω , the coupling to gravity:

$$c = -\frac{m_0^2 \ddot{\Omega}}{2a^2} + \frac{m_0^2 \mathcal{H} \dot{\Omega}}{a^2} + \frac{m_0^2 (1 + \Omega)}{a^2} (\mathcal{H}^2 - \dot{\mathcal{H}}) - \frac{1}{2} (\rho_m + P_m) \tag{A.6}$$

$$\Lambda = -\frac{m_0^2 \ddot{\Omega}}{a^2} - \frac{m_0^2 \mathcal{H} \dot{\Omega}}{a^2} - \frac{m_0^2 (1 + \Omega)}{a^2} (\mathcal{H}^2 + 2\dot{\mathcal{H}}) - P_m, \tag{A.7}$$

where ρ_m and P_m are the matter energy density and pressure, respectively [14, 15]. EFTCAMB multiplies R by $1 + \Omega$ rather than Ω for numerical accuracy. $S_m[\chi_i, g_{\mu\nu}]$ is the action for all matter fields χ_i .

The Stückelberg technique makes the scalar perturbations explicit in unitary gauge. The conformal time is perturbed by a scalar field π , known as the Stückelberg field. All equations are now functions of $\tau + \pi$, and the perturbation operators transform as [14, 15]

$$\delta g^{00} \rightarrow \delta g^{00} - 2 \frac{\dot{\pi}^2}{a^2} - 2 \frac{\mathcal{H} \pi}{a^2} + \dots \tag{A.8}$$

$$\delta K^\mu{}_\nu \rightarrow \delta K^\mu{}_\nu + \frac{\dot{\mathcal{H}}}{a} \pi \delta^\mu{}_\nu + \frac{1}{a^2} \bar{\nabla}^\mu \bar{\nabla}_\nu \pi + \dots \tag{A.9}$$

$$\delta R^{(3)} \rightarrow \delta R^{(3)} + 4 \frac{\mathcal{H}}{a} \bar{\nabla}^2 \pi + \dots \tag{A.10}$$

The Horndeski theory of gravity is the most general tensor-scalar theory in which the equations of motion are second order [1]. However, the authors of [4] and [50] have presented an extended Horndeski theory in which the equations of motion have higher order

derivatives. The equations of motion that describe the propagating degrees of freedom reduce to second order equations and, thus, avoid Ostrogradski instabilities [see also 51, 52]. In this study we restrict ourselves to ordinary Horndeski theory in which operators contain at most two derivatives. The authors of [53] detail the derivatives introduced by the perturbation operators that act on the metric and scalar field perturbations. They note both $(K^\mu{}_\mu)^2$ and $\delta K^\mu{}_\nu \delta K^\nu{}_\mu$ contain terms with four spatial derivatives on the scalar perturbations and with one time and two spatial derivatives. Cancelling the two operators removes the four spatial derivatives, while $\delta g^{00} \delta R^{(3)}$ can cancel with the mixed time and spatial derivative term. The $\partial_\mu (a^2 g^{00}) \partial_\nu (a^2 g^{00})$ term also contains higher order derivatives that cannot cancel with any other term, so it must be removed. The coefficient relationships required for these cancellations to occur are [53]

$$2\hat{M}^2 = \bar{M}_2^2 = -\bar{M}_3^2 \quad \text{and} \quad m_2 = 0. \quad (\text{A.11})$$

The authors of [2] have formulated a physically motivated parameterization of the coefficients in the action displayed in Equation A.1 for Horndeski theory. The following four parameters are independent of both themselves and the background:

$$\alpha_K = \frac{2ca^2 + 4M_2^4 a^2}{m_0^2 \mathcal{H}^2 (1 + \Omega + \bar{M}_2^2/m_0^2)}, \quad (\text{A.12})$$

$$\alpha_B = + \frac{a\bar{M}_1^3/m_0^2 + a\mathcal{H}\Omega'}{2\mathcal{H} (1 + \Omega + \bar{M}_2^2/m_0^2)}, \quad (\text{A.13})$$

$$\alpha_T = - \frac{\bar{M}_2^2}{m_0^2 (1 + \Omega) + \bar{M}_2^2}, \quad (\text{A.14})$$

$$\text{and} \quad \alpha_M = a \frac{d \ln M_*^2}{da} = \frac{a (\Omega + \bar{M}_2^2/m_0^2)'}{1 + \Omega + \bar{M}_2^2/m_0^2}, \quad (\text{A.15})$$

where primes denote derivatives with respect to the scale factor a . In our work we choose a Λ CDM background. EFTCAMB evolves $M_*^2/m_0^2 = 1 + \widetilde{M} = 1 + \Omega + \bar{M}_2^2/m_0^2$ for numerical reasons, transforming Equation A.15 to $\alpha_M = a\widetilde{M}' / (1 + \widetilde{M})$.

B Effects of Kineticity on Stability Constraints

Kineticity's effects on the observables are closely related to the accuracy of the quasi-static approximation. The authors of [54] have shown that when analyzing the CMB, the quasi-static limit should be used neither when dark energy has a non-negligible effect at recombination nor when modeling the integrated Sachs-Wolfe (ISW) effect. If the dark energy sound speed, also known as the π field sound speed, is less than 0.1, the quasi-static limit is not valid for CMB lensing. When the approximation is valid, kineticity does not enter the equations of motion and is not well constrained by observations. As mentioned in Section 2, Ref. [12] found that α_K could not be well constrained with their parameterization. They then presented constraints on α_T , α_M , and α_B for a few fixed values of kineticity. To limit the number of additional degrees of freedom in our analysis, we also fix α_0^K in our analysis.

With $\alpha_0^T = 0$, we find that evolving the remaining parameters as constants, with $\alpha_K = 0.1$, yields a stable parameter space too small to explore with an MCMC analysis. Evolving the Horndeski parameters as power laws (see Section 2 and Appendix C) enlarges the stable parameter space and provides the opportunity to probe the time evolution of the parameters.

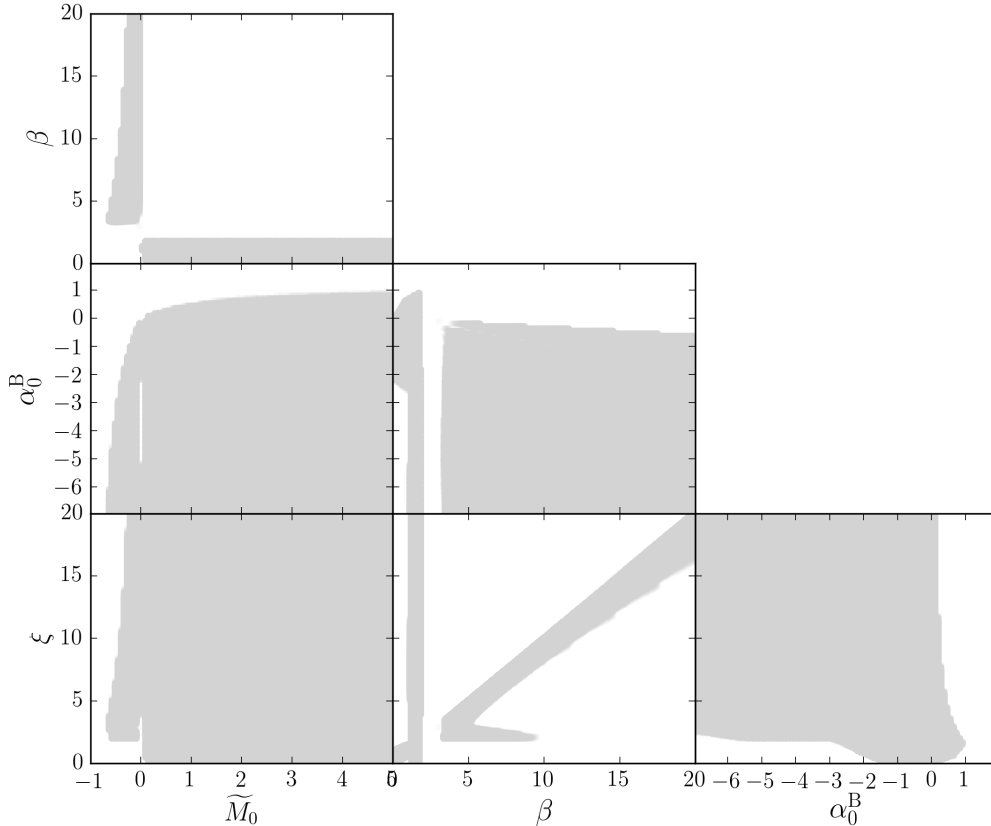


Figure 8. Stable parameter space when $\alpha_K = 0.1a^3$.

Although the authors of [12] found the remaining Horndeski parameters have a weak dependence on kineticity, we note that fixing the kineticity has non-trivial effects on our viable parameter space. We believe this is primarily due to the tachyon instabilities defined in Section 3. In Figure 8 we explore the stable parameter space for $\alpha_0^K = 0.1$. We fix $\kappa = 3.0$, which we found provides a large range of likely values for the other Horndeski parameters. The stable region for β , the power law index related to friction, has a gap from $2 \lesssim \beta \lesssim 3$ due to mathematical stability conditions. Without using a nested sampling method, the MCMC cannot reach both stable β regions. We choose to only explore the smaller friction exponent values $\beta \lesssim 2$ since large values will drive the friction parameter α_M close to 0. Having $\widetilde{M}_0 \approx 0$ effectively achieves the same result if the data prefer $\alpha_M \approx 0$.

Stability requires the scalar propagation speed to satisfy [2]

$$c_s^2 = -\frac{2(1 + \alpha_B) \left[\dot{\mathcal{H}} - (1 - \alpha_B + \alpha_M) \mathcal{H}^2 \right] + 2\mathcal{H}\dot{\alpha}_B + a^2(\tilde{\rho}_m + \tilde{p}_m)}{H^2(\alpha_K + 6\alpha_B^2)} > 0, \quad (\text{B.1})$$

using the definition for α_B of [34]. Because both kineticity and braiding are in the denominator, it is not stable to have $\alpha_0^K = 0$ and $\alpha_0^B = 0$ simultaneously. Thus, to explore the $\alpha_0^B = 0$

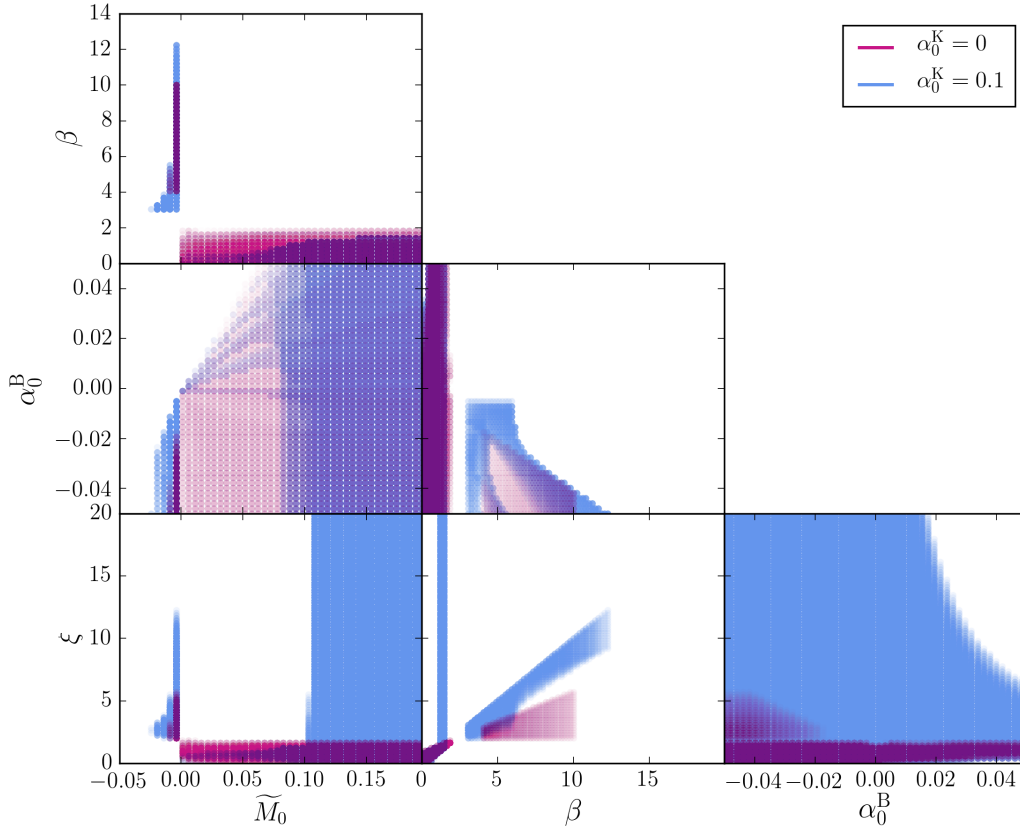


Figure 9. Comparison between the stable parameter spaces for $\alpha_0^K = 0$ and $\alpha_0^K = 0.1$ when α_0^B is near 0.

case and compare with the $\alpha_0^B \neq 0$ case in a self-consistent manner, we must fix α_0^K at a nonzero value.

We analyzed the stable parameter space for $\alpha_0^K = 0$ and $\alpha_0^K = 1.0$, as well. Increasing α_0^K from 0.1 to 1.0 significantly shrinks the stable parameter space to the extent it cannot be explored with an MCMC analysis. We fix $\alpha_0^K = 0.1$ throughout our analysis due to its larger stable parameter space and closeness to GR.

In [Figure 9](#) we compare the stable parameter space for $\alpha_0^K = 0$ and $\alpha_0^K = 0.1$ for values near $\alpha_0^B = 0$. The higher the point opacity the larger the stable parameter space allowed by the parameter values describing that point. Regions of overlap indicate where parameters are stable for both kineticity values. The difference in the stable parameter space for the two kineticity values is dramatic, indicating the importance of understanding how all imposed stability conditions affect the viable parameter space to correctly interpret the parameter posteriors. When $\alpha_0^K = 0.1$, the viable parameter space when $0 \lesssim \widetilde{M}_0 \lesssim 0.1$ is small, whereas for $\alpha_0^K = 0$ the same \widetilde{M}_0 values provide a larger stable parameter space. The tachyon stability conditions solely drive these differences and those in the other stability contours. For the $\alpha_0^K = 0.1$ case, the viable $\widetilde{M}_0 - \alpha_0^B$ space converges to a single point as both α_0^B and

\widetilde{M}_0 approach 0^+ , i.e. their GR value from the right. Thus, the choice of kineticity affects the \widetilde{M}_0 posterior due to the tachyon stability constraints (see Section 4). Indeed, if we remove the mathematical stability conditions the viable parameter spaces for $\alpha_0^K = 0$ and $\alpha_0^K = 0.1$ are identical.

We also note that while the stability contours for $\alpha_0^K = 0$ make it appear $\alpha_0^B = 0$ is stable for this kineticity, there are no stable points when both $\alpha_0^K = 0$ and $\alpha_0^B = 0$ *exactly*. The appearance of the plot is an artifact of discretely sampling the parameter space.

C Parameter Evolution

To better constrain the Horndeski parameters we explore the pivot point a_* at which to measure the parameters. The parameters of interest to measure then become

$$\alpha_*^B = \alpha_0^B a_*^\xi \quad (\text{C.1})$$

$$\alpha_*^M = \widetilde{M}_0 a_*^\beta \frac{\beta}{1 + \widetilde{M}_0 a_*^\beta} \quad (\text{C.2})$$

along with their exponents ξ and β . We are then evolving

$$\alpha_B = \alpha_*^B \left(\frac{a}{a_*} \right)^\xi \quad (\text{C.3})$$

$$\alpha_M = \alpha_*^M \left(\frac{a}{a_*} \right)^\beta \frac{\beta}{\beta + \left[(a/a_*)^\beta - 1 \right] \alpha_*^M}. \quad (\text{C.4})$$

We can derive the braiding and friction today, α_0^B and $\widetilde{M}_0 \beta / (1 + \widetilde{M}_0)$, respectively, from these measured values. In Figure 10 we show the correlation coefficient between Horndeski parameters of interest as well as σ_8 as a function of pivot redshift z_* . α_*^B is relatively uncorrelated with the other parameters at decoupling, which could be an artifact of the power law evolution. α_*^M and σ_8 are positively correlated at present. This is consistent with the effects seen in the matter power spectrum when increasing \widetilde{M}_0 (see Section 5). Large scales entered the horizon at low redshifts when α_*^M and σ_8 were positively correlated. Hence, increasing \widetilde{M}_0 creates an amplifying effect on large scales. α_*^B and α_*^M are positively correlated with their respective exponents at the present epoch. However, the only epoch during which α_*^B and α_*^M are uncorrelated is at present.

α_*^B has the smallest relative uncertainty at present. The relative uncertainty for α_*^M has a small minimum near $z_* \approx 10 - 20$, similar redshifts to where α_*^M is uncorrelated with β and σ_8 . This suggests a pivot point earlier than the present may be preferable for α_M . However, the relative uncertainty for α_*^M at present is almost as small. Thus, because α_*^B and α_*^M are uncorrelated at present and the relative uncertainties for each are minimized or close to the minimum, we choose to keep the pivot point at present.

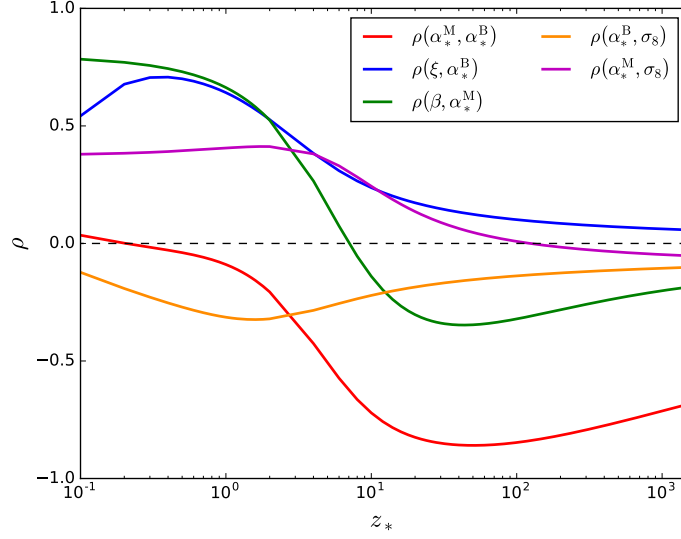


Figure 10. Correlation coefficients for the Horndeski parameters derived from the CMB+LSS chains.

References

- [1] G. W. Horndeski, *Second-Order Scalar-Tensor Field Equations in a Four-Dimensional Space*, *International Journal of Theoretical Physics* **10** (Sept., 1974) 363–384.
- [2] E. Bellini and I. Sawicki, *Maximal freedom at minimum cost: linear large-scale structure in general modifications of gravity*, *J. Cosmology Astropart. Phys.* **7** (July, 2014) 50, [[1404.3713](#)].
- [3] B. P. Abbott, R. Abbott, T. D. Abbott, F. Acernese, K. Ackley, C. Adams et al., *Gravitational waves and gamma-rays from a binary neutron star merger: Gw170817 and grb 170817a*, *The Astrophysical Journal Letters* **848** (2017) L13.
- [4] M. Zumalacárregui and J. García-Bellido, *Transforming gravity: From derivative couplings to matter to second-order scalar-tensor theories beyond the Horndeski Lagrangian*, *Phys. Rev. D* **89** (Mar., 2014) 064046, [[1308.4685](#)].
- [5] L. Lombriser and A. Taylor, *Breaking a dark degeneracy with gravitational waves*, *J. Cosmology Astropart. Phys.* **3** (Mar., 2016) 031, [[1509.08458](#)].
- [6] L. Lombriser and N. A. Lima, *Challenges to self-acceleration in modified gravity from gravitational waves and large-scale structure*, *Physics Letters B* **765** (Feb., 2017) 382–385, [[1602.07670](#)].
- [7] J. María Ezquiaga and M. Zumalacárregui, *Dark Energy after GW170817*, *ArXiv e-prints* (Oct., 2017) , [[1710.05901](#)].
- [8] P. Creminelli and F. Vernizzi, *Dark Energy after GW170817*, *ArXiv e-prints* (Oct., 2017) , [[1710.05877](#)].
- [9] T. Baker, E. Bellini, P. G. Ferreira, M. Lagos, J. Noller and I. Sawicki, *Strong constraints on cosmological gravity from GW170817 and GRB 170817A*, *ArXiv e-prints* (Oct., 2017) , [[1710.06394](#)].
- [10] S. Arai and A. Nishizawa, *Generalized framework for testing gravity with gravitational-wave propagation. II. Constraints on Horndeski theory*, *ArXiv e-prints* (Nov., 2017) , [[1711.03776](#)].

- [11] C. Deffayet, O. Pujolàs, I. Sawicki and A. Vikman, *Imperfect dark energy from kinetic gravity braiding*, *J. Cosmology Astropart. Phys.* **10** (Oct., 2010) 26, [[1008.0048](#)].
- [12] E. Bellini, A. J. Cuesta, R. Jimenez and L. Verde, *Constraints on deviations from Λ CDM within Horndeski gravity*, *ArXiv e-prints* (Sept., 2015) , [[1509.07816](#)].
- [13] D. Bettoni and M. Zumalacárregui, *Kinetic mixing in scalar-tensor theories of gravity*, *Phys. Rev. D* **91** (May, 2015) 104009, [[1502.02666](#)].
- [14] B. Hu, M. Raveri, N. Frusciante and A. Silvestri, *Effective field theory of cosmic acceleration: An implementation in CAMB*, *Phys. Rev. D* **89** (May, 2014) 103530, [[1312.5742](#)].
- [15] M. Raveri, B. Hu, N. Frusciante and A. Silvestri, *Effective field theory of cosmic acceleration: Constraining dark energy with CMB data*, *Phys. Rev. D* **90** (Aug., 2014) 043513, [[1405.1022](#)].
- [16] A. Lewis, A. Challinor and A. Lasenby, *Efficient Computation of Cosmic Microwave Background Anisotropies in Closed Friedmann-Robertson-Walker Models*, *ApJ* **538** (Aug., 2000) 473–476, [[astro-ph/9911177](#)].
- [17] A. Lewis and S. Bridle, *Cosmological parameters from CMB and other data: A Monte Carlo approach*, *Phys. Rev. D* **66** (Nov., 2002) 103511, [[astro-ph/0205436](#)].
- [18] A. Gelman and D. B. Rubin, *Inference from Iterative Simulation Using Multiple Sequences*, *Statistical Science* **7** (1992) 457–472.
- [19] Planck Collaboration, P. A. R. Ade, N. Aghanim, M. Arnaud, M. Ashdown, J. Aumont et al., *Planck 2015 results. XIV. Dark energy and modified gravity*, *ArXiv e-prints* (Feb., 2015) , [[1502.01590](#)].
- [20] E. V. Linder, *Challenges in connecting modified gravity theory and observations*, *Phys. Rev. D* **95** (Jan., 2017) 023518, [[1607.03113](#)].
- [21] J. Gleyzes, *Parametrizing modified gravity for cosmological surveys*, *Phys. Rev. D* **96** (Sept., 2017) 063516, [[1705.04714](#)].
- [22] E. Bellini, A. J. Cuesta, R. Jimenez and L. Verde, *Erratum: Constraints on deviations from Λ CDM within Horndeski gravity* *Erratum: Constraints on deviations from Λ CDM within Horndeski gravity*, *J. Cosmology Astropart. Phys.* **6** (June, 2016) E01.
- [23] L. Amendola, G. Ballesteros and V. Pettorino, *Effects of modified gravity on B-mode polarization*, *Phys. Rev. D* **90** (Aug., 2014) 043009, [[1405.7004](#)].
- [24] M. Raveri, C. Baccigalupi, A. Silvestri and S.-Y. Zhou, *Measuring the speed of cosmological gravitational waves*, *Phys. Rev. D* **91** (Mar., 2015) 061501, [[1405.7974](#)].
- [25] V. Pettorino and L. Amendola, *Friction in gravitational waves: A test for early-time modified gravity*, *Physics Letters B* **742** (Mar., 2015) 353–357, [[1408.2224](#)].
- [26] BICEP2/Keck and Planck Collaborations, P. A. R. Ade, N. Aghanim, Z. Ahmed, R. W. Aikin, K. D. Alexander et al., *Joint Analysis of BICEP2/Keck Array and Planck Data*, *Physical Review Letters* **114** (Mar., 2015) 101301, [[1502.00612](#)].
- [27] Planck Collaboration, N. Aghanim, M. Arnaud, M. Ashdown, J. Aumont, C. Baccigalupi et al., *Planck 2015 results. XI. CMB power spectra, likelihoods, and robustness of parameters*, *A&A* **594** (Sept., 2016) A11, [[1507.02704](#)].
- [28] Planck Collaboration, P. A. R. Ade, N. Aghanim, M. Arnaud, M. Ashdown, J. Aumont et al., *Planck 2015 results. XV. Gravitational lensing*, *A&A* **594** (Sept., 2016) A15, [[1502.01591](#)].
- [29] M. Tegmark, D. J. Eisenstein, M. A. Strauss, D. H. Weinberg, M. R. Blanton, J. A. Frieman et al., *Cosmological constraints from the SDSS luminous red galaxies*, *Phys. Rev. D* **74** (Dec., 2006) 123507, [[astro-ph/0608632](#)].
- [30] L. Anderson, É. Aubourg, S. Bailey, F. Beutler, V. Bhardwaj, M. Blanton et al., *The clustering of galaxies in the SDSS-III Baryon Oscillation Spectroscopic Survey: baryon acoustic*

- oscillations in the Data Releases 10 and 11 Galaxy samples*, *MNRAS* **441** (June, 2014) 24–62, [[1312.4877](#)].
- [31] A. J. Ross, L. Samushia, C. Howlett, W. J. Percival, A. Burden and M. Manera, *The clustering of the SDSS DR7 main Galaxy sample - I. A 4 per cent distance measure at $z = 0.15$* , *MNRAS* **449** (May, 2015) 835–847, [[1409.3242](#)].
- [32] F. Beutler, C. Blake, M. Colless, D. H. Jones, L. Staveley-Smith, G. B. Poole et al., *The 6dF Galaxy Survey: $z \approx 0$ measurements of the growth rate and σ_8* , *MNRAS* **423** (July, 2012) 3430–3444, [[1204.4725](#)].
- [33] L. Samushia, B. A. Reid, M. White, W. J. Percival, A. J. Cuesta, G.-B. Zhao et al., *The clustering of galaxies in the SDSS-III Baryon Oscillation Spectroscopic Survey: measuring growth rate and geometry with anisotropic clustering*, *MNRAS* **439** (Apr., 2014) 3504–3519, [[1312.4899](#)].
- [34] B. Hu, M. Raveri, N. Frusciante and A. Silvestri, *EFTCAMB/EFTCosmoMC: Numerical Notes v2.0*, *ArXiv e-prints* (May, 2014) , [[1405.3590](#)].
- [35] A. De Felice, N. Frusciante and G. Papadomanolakis, *On the stability conditions for theories of modified gravity in the presence of matter fields*, *J. Cosmology Astropart. Phys.* **3** (Mar., 2017) 027, [[1609.03599](#)].
- [36] M. Zumalacárregui, E. Bellini, I. Sawicki, J. Lesgourgues and P. G. Ferreira, *hi_class: Horndeski in the Cosmic Linear Anisotropy Solving System*, *J. Cosmology Astropart. Phys.* **8** (Aug., 2017) 019, [[1605.06102](#)].
- [37] A. Adams, N. Arkani-Hamed, S. Dubovsky, A. Nicolis and R. Rattazzi, *Causality, analyticity and an IR obstruction to UV completion*, *Journal of High Energy Physics* **10** (Oct., 2006) 014, [[hep-th/0602178](#)].
- [38] D. A. Easson, I. Sawicki and A. Vikman, *When matter matters*, *J. Cosmology Astropart. Phys.* **7** (July, 2013) 014, [[1304.3903](#)].
- [39] M. Raveri. Personal Communication, 2016.
- [40] V. Salvatelli, F. Piazza and C. Marinoni, *Constraints on modified gravity from Planck 2015: when the health of your theory makes the difference*, *ArXiv e-prints* (Feb., 2016) , [[1602.08283](#)].
- [41] J. Sakstein and B. Jain, *Implications of the Neutron Star Merger GW170817 for Cosmological Scalar-Tensor Theories*, *ArXiv e-prints* (Oct., 2017) , [[1710.05893](#)].
- [42] Planck Collaboration, P. A. R. Ade, N. Aghanim, M. Arnaud, M. Ashdown, J. Aumont et al., *Planck 2015 results. XIII. Cosmological parameters*, *ArXiv e-prints* (Feb., 2015) , [[1502.01589](#)].
- [43] J. Renk, M. Zumalacarregui and F. Montanari, *Gravity at the horizon: on relativistic effects, CMB-LSS correlations and ultra-large scales in Horndeski’s theory*, *ArXiv e-prints* (Apr., 2016) , [[1604.03487](#)].
- [44] W. Lin and M. Ishak, *Testing gravity theories using tensor perturbations*, *ArXiv e-prints* (May, 2016) , [[1605.03504](#)].
- [45] H. Akaike, *A New Look at the Statistical Model Identification*, *IEEE Transactions on Automatic Control* **19** (1974) 716–723.
- [46] T. Giannantonio and E. Komatsu, *Bayesian evidence of nonstandard inflation: Isocurvature perturbations and running spectral index*, *Phys. Rev. D* **91** (Jan., 2015) 023506, [[1407.4291](#)].
- [47] C. Cheung, A. L. Fitzpatrick, J. Kaplan, L. Senatore and P. Creminelli, *The effective field theory of inflation*, *Journal of High Energy Physics* **3** (Mar., 2008) 14–014, [[0709.0293](#)].
- [48] G. Gubitosi, F. Piazza and F. Vernizzi, *The effective field theory of dark energy*, *J. Cosmology Astropart. Phys.* **2** (Feb., 2013) 32, [[1210.0201](#)].

- [49] J. Bloomfield, É. É. Flanagan, M. Park and S. Watson, *Dark energy or modified gravity? An effective field theory approach*, *J. Cosmology Astropart. Phys.* **8** (Aug., 2013) 10, [[1211.7054](#)].
- [50] J. Gleyzes, D. Langlois, F. Piazza and F. Vernizzi, *Healthy theories beyond Horndeski*, *ArXiv e-prints* (Apr., 2014) , [[1404.6495](#)].
- [51] J. Gleyzes, D. Langlois, F. Piazza and F. Vernizzi, *Exploring gravitational theories beyond Horndeski*, *J. Cosmology Astropart. Phys.* **2** (Feb., 2015) 18, [[1408.1952](#)].
- [52] C. Lin, S. Mukohyama, R. Namba and R. Saitou, *Hamiltonian structure of scalar-tensor theories beyond Horndeski*, *J. Cosmology Astropart. Phys.* **10** (Oct., 2014) 71, [[1408.0670](#)].
- [53] J. Bloomfield, *A simplified approach to general scalar-tensor theories*, *J. Cosmology Astropart. Phys.* **12** (Dec., 2013) 44, [[1304.6712](#)].
- [54] I. Sawicki and E. Bellini, *Limits of quasistatic approximation in modified-gravity cosmologies*, *Phys. Rev. D* **92** (Oct., 2015) 084061, [[1503.06831](#)].